

# Algorithms for Improving Calculated Streamlines in 3-D Phase Contrast Angiography

Michael H. Buonocore

Streamline display is a unique alternative to cross-sectional slice or projection display, because streamlines more clearly show the patterns of blood flow within the vessel. Flow patterns associated with atherosclerosis, such as streamline separation and recirculation, can be quickly identified with this display. Streamlines can be calculated using velocity data obtained from 3-D phase contrast angiographic pulse sequences. However, these streamlines often pass through the wall of vessel or show intraluminal sources and sinks of blood. The author has developed iterative least squares algorithms to improve the realism of streamlines. The velocity data is modified so that the resulting streamlines do not pass through the vessel wall and there are no intraluminal sources or sinks. He has applied the algorithms to velocity data obtained from a flow phantom and the carotid arteries of normal volunteers. Streamlines derived from the processed velocity fields are more realistic and provide more precise flow quantitation.

**Key words:** 3-D image processing; phase contrast angiography; flow streamlines; atherosclerosis.

## INTRODUCTION

Streamlines allow rapid assessment of spatial and temporal blood flow patterns. Their clinical importance is that streamline separation and recirculation is correlated with genesis of atherosclerosis (1). If streamline visualization were readily available in the clinical setting, it could be used in subjects with vascular abnormalities to rapidly locate regions of streamline separation, recirculation and other potentially pathogenic flow patterns. Streamlines can be generated using velocity data from 3-D phase contrast MR angiography (2). However, the streamlines calculated from raw velocity data, especially in regions of high velocities, may be unrealistic in that they may pass through the walls of the vessel or show sources and sinks of blood within the lumen. Velocity fields from 3-D phase contrast angiography should obey fluid dynamics' constraints; they should be divergence-free, have constant flow through adjacent cross sectional

surfaces, and generate streamlines that do not pass through the vessel walls. Algorithms have been developed to minimally modify 3-D velocity fields such that the resulting velocity field is consistent with these constraints. Streamlines derived from these modified velocity fields are more realistic and provide more precise flow quantitation.

## METHODS

Velocity data was obtained from a curved tube flow phantom and in the carotid arteries of three normal subjects. All subjects gave informed consent. The phantom consisted of one curved section of 1-inch I.D. vinyl tubing. (Fig. 1). A peristaltic pump drove the  $\text{MnCl}_2$  doped water ( $T_1 = 850$  ms) through the tubes at 1610.0 cc/min (26.833 cc/s)  $\pm 0.25\%$  corresponding to a mean velocity of 6.237 cm/s. The mean velocity of the flow driven by the pump varied less than 3% of its mean through the pump cycle. 3-D phase contrast angiography (G.E. Medical Systems, Signa version 4.7) was done with  $TR = 27$ ,  $TE = 10.1$ ,  $FA = 20^\circ$ , 14 cm FOV,  $256 \times 256$  matrix, 1.3 mm slice, 28 slices,  $VENC = 30$  cm/s using 6-point balanced encoding, Flow comp, A/P frequency encode. Axial cross sections of amplitude (i.e., magnitude of complex signal), S/I, A/P, and R/L velocity encoded phase images showed the posterior to anterior flow and a region of recirculation in the curved section. Velocity data at the carotid artery bifurcation was obtained using parameters  $TR = 27$ ,  $TE = 10.1$ ,  $FA = 20^\circ$ , 12 cm FOV,  $256 \times 256$  matrix, 1.0 mm slice, 28 slices,  $VENC = 70$  cm/s S/I direction, 40 cm/s R/L and A/P directions, Flow comp, A/P frequency encode. 40 cm/s encoding was obtained using 6-point balanced encoding. 70 cm/s encoding in S/I direction was obtained by running an additional 2-point balanced scan. This was necessary to better match the encoding to the prevailing velocities in each direction, and thereby improve velocity measurement S/N (3).

Three interrelated algorithms were developed to correct a) the background (zero velocity) value, b) divergence, and c) flow-through-wall, of the unprocessed velocity field. The *background correction* algorithm removed the residual background trend typically found in velocity encoded phase images. The *divergence correction* algorithm iteratively reduced the calculated divergence of the velocity field at each point. The *flow-through-wall correction* algorithm set the velocity component at the wall boundary points to zero. The wall

MRM 31:22-30 (1994)

From the Department of Radiology, UC Davis Medical Center, Sacramento, California.

Address correspondence to: Michael H. Buonocore, M.D., Ph.D., Division of Diagnostic Radiology, TICON-II, 2nd Floor, UC Davis Medical Center, Sacramento, CA 95817.

Received June 18, 1993; revised August 31, 1993; accepted August 31, 1993.

This work was supported in part by a grant from the Whitaker Foundation. 0740-3194/94 \$3.00

Copyright © 1994 by Williams & Wilkins

All rights of reproduction in any form reserved.

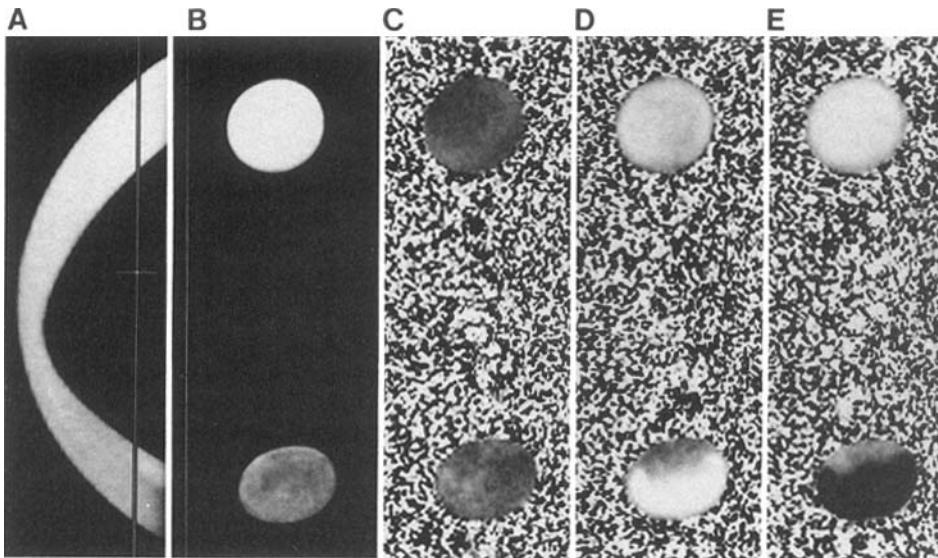


FIG. 1. (A) Sagittal maximum intensity projection of amplitude images of curved tube flow phantom. Flow direction of  $\text{MnCl}_2$ -doped water was from bottom of picture (posterior) to top of picture (anterior). Vertical line in (A) indicates location of axial images. (B) Axial amplitude image. (C) Axial  $V_x$  (right/left) encode. (D)  $V_y$  (anterior/posterior) encode. (E) Axial  $V_z$  (superior/inferior) encode.

boundary was determined from the amplitude images. At each boundary point, the image intensity gradient specified the direction normal to the boundary. On the amplitude images, threshold criteria were set to establish that the point was inside the vessel. Additional thresholds were set for the magnitude of the gradient to establish that the point was near the boundary. Streamlines were generated using a first order integration of the velocity field with a fixed time step chosen so that about 10% of a voxel width was traversed each step. The color at each point along the streamline indicated the time for the blood to travel along the streamline to that point.

Background trends were typically linear and varied about  $\pm 2$  to  $\pm 20$  pixel units across the image. These variations can significantly effect flow measurement accuracy (4). The background correction algorithm adjusted each velocity component by a linear function of the spatial coordinates. Pixel values gave velocities in mm/s directly. At each pixel, the background value was subtracted from these pixel values to give an adjusted velocity in mm/s. In the flow phantom, flow measurements were computed from the velocity field at  $N$  cross sections drawn at preselected points along the tube (Fig. 2). The coefficients of the linear functions were computed by least squares to minimize the difference between the flow measurements at the cross-sections (Table 1). The flow through the cross-sections was also set to be equal to the actual flow determined from the physical flowmeter. The vessel wall was included in the least squares problem as an additional surface through which the net flow was ideally zero. After each background correction, the velocity field was updated, and new cross sectional surfaces were drawn perpendicular to the updated velocity field. Iteration was stopped when the background linear functions and cross-section orientations did not change visually. For the carotid artery angiograms, this background correction technique was not done. Instead, the background was determined by searching the amplitude and phase images of the entire 3-D image set for pixels satisfying a "no-flow" criterion. Pix-

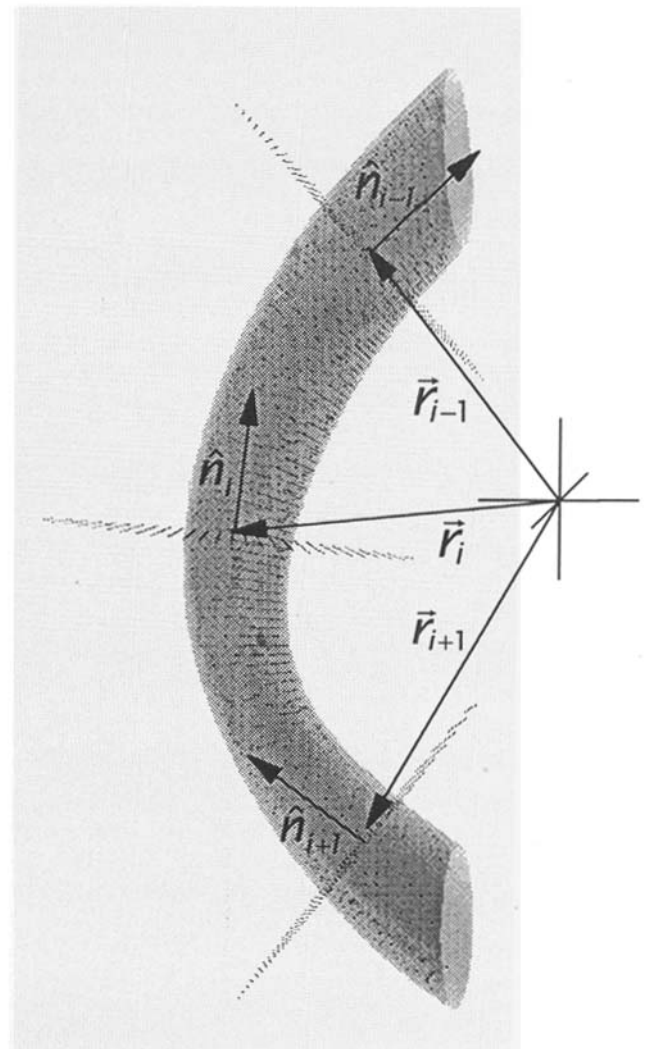


FIG. 2. Each cross-section drawn at a preselected central voxel in the curved tube was perpendicular to the velocity at the voxel. The wall of the curved tube was used as a surface through which the net flow is ideally zero.

Table 1  
Definitions and Equations for Background Correction Algorithm

|                                                                                                                                                                                                                                                                                                                                                                                                                                                                                                 |                                                                                                                                                                                                                                                                                                                                                                                                                                                                                                             |
|-------------------------------------------------------------------------------------------------------------------------------------------------------------------------------------------------------------------------------------------------------------------------------------------------------------------------------------------------------------------------------------------------------------------------------------------------------------------------------------------------|-------------------------------------------------------------------------------------------------------------------------------------------------------------------------------------------------------------------------------------------------------------------------------------------------------------------------------------------------------------------------------------------------------------------------------------------------------------------------------------------------------------|
| <p>Cost function:</p> $C = \sum_{i=1}^N \left( \frac{(\hat{n}_i \cdot \tilde{v}_i) - e_i}{(\text{area})_i} \right)^2$ $= \sum_{i=1}^N \left( n_{xi}(a_{xx}x + a_{yx}y + a_{zx}z + v_{x0}) + n_{yi}(a_{xy}x + a_{yy}y + a_{zy}z + v_{y0}) + n_{zi}(a_{xz}x + a_{yz}y + a_{zz}z + v_{z0}) - \frac{e_i}{\text{area}_i} \right)^2$ <p>Linear equations:</p> $\frac{\partial C}{\partial v_{k0}} = 0 \quad k = 1, 2, 3$ $\frac{\partial C}{\partial a_{kl}} = 0 \quad k = 1, 2, 3 \quad l = 1, 2, 3$ | <p>Definitions:</p> $\tilde{v}_i \equiv (v_{xi} \quad v_{yi} \quad v_{zi})$ velocity, c - s #i<br>$\tilde{r}_i \equiv (r_{xi} \quad r_{yi} \quad r_{zi})$ position, c - s #i<br>$\hat{n}_i \equiv (n_{xi} \quad n_{yi} \quad n_{zi})$ normal, c - s #i<br>$\tilde{a}_x \equiv (a_{xx} \quad a_{yx} \quad a_{zx})$<br>$\tilde{a}_y \equiv (a_{xy} \quad a_{yy} \quad a_{zy})$<br>$\tilde{a}_z \equiv (a_{xz} \quad a_{yz} \quad a_{zz})$<br>$\tilde{v}_0 \equiv (v_{x0} \quad v_{y0} \quad v_{z0})$          |
|                                                                                                                                                                                                                                                                                                                                                                                                                                                                                                 | <p>Model:</p> $\left. \begin{aligned} v_{xi} &= \tilde{a}_x \cdot \tilde{r}_i + v_{x0} \\ v_{yi} &= \tilde{a}_y \cdot \tilde{r}_i + v_{y0} \\ v_{zi} &= \tilde{a}_z \cdot \tilde{r}_i + v_{z0} \end{aligned} \right\} \begin{array}{l} \text{velocity} \\ \text{correction at} \\ \text{c - s \#i} \end{array}$ <p><math>e_i</math> = error in flux, c - s #i<br/> <math>\text{area}_i</math> = area, c - s #i<br/> <math>\text{area}_i(\hat{n}_i \cdot \tilde{v}_i)</math> = flow correction, c - s #i</p> |

els above a certain brightness on the amplitude image and above a minimum phase angle on the phase image were designated as having flowing spins. Both phase and amplitude criteria were required to provide an adequate segmentation of vessel and background pixels. Pixels in the amplitude images below a certain threshold were considered to have a noisy phase angle (5), and were not included in the background calculation. Cutoffs were selected empirically by the user by graphically displaying the selected background pixels and confirming that regions of major vessels, bone and air were excluded. The values of the selected background pixels were fit to a linear function of the spatial parameters.

Water and blood were each modeled as incompressible fluids (6). Therefore, the local divergence of the velocity field should have been zero. At each grid point, the divergence correction algorithm applied a first-order correction based on the spatial derivative of the divergence of the velocity field to bring the divergence to the same

value at every grid point in the vessel. The algorithm acted on the grid points within the vessel sequentially and was run across the grid multiple times. Table 2 shows that the x-derivative of the divergence,  $\partial/\partial x(\tilde{\nabla} \cdot \tilde{V})$ , at grid point  $(i, j, k)$  is selectively reduced by updating  $V_x(i, j, k)$ . Updates of  $V_y(i, j, k)$  and  $V_z(i, j, k)$  were used to selectively reduce  $\partial/\partial y(\tilde{\nabla} \cdot \tilde{V})$  and  $\partial/\partial z(\tilde{\nabla} \cdot \tilde{V})$ , respectively, without affecting the reduction of  $\partial/\partial x(\tilde{\nabla} \cdot \tilde{V})$ . Background correction was run immediately after divergence correction to eliminate the uniform non-zero divergence.

Flow through the wall at each boundary point was determined by the velocity component parallel to the boundary gradient. This velocity component was multiplied by the effective cross-sectional area of the wall surface at each boundary point. The flow-through-wall correction algorithm set this velocity component to zero. Both divergence and background corrections were applied immediately after this correction to restore zero

Table 2  
Definitions and Equations for Divergence Correction Algorithm

For  $V_x$  update:

$$\begin{aligned} \frac{\partial}{\partial x} \tilde{\nabla} \cdot \tilde{V} &= \frac{\partial}{\partial x} \left( \frac{\partial V_x}{\partial x} + \frac{\partial V_y}{\partial y} + \frac{\partial V_z}{\partial z} \right) \\ &\equiv \frac{V_x(i+1, j, k) - 2 * \overset{\text{updated term}}{V_x(i, j, k)} + V_x(i-1, j, k)}{dx * dx} \\ &\quad + \frac{(V_y(i+1, j+1, k) - V_y(i-1, j+1, k)) - (V_y(i+1, j-1, k) - V_y(i-1, j-1, k))}{2 * dx * 2 * dy} \\ &\quad + \frac{(V_z(i+1, j, k+1) - V_z(i-1, j, k+1)) - (V_z(i+1, j, k-1) - V_z(i-1, j, k-1))}{2 * dx * 2 * dz} \end{aligned} \quad \left. \begin{array}{l} \frac{\partial}{\partial x} \left( \frac{\partial V_x}{\partial x} \right) \\ \frac{\partial}{\partial x} \left( \frac{\partial V_y}{\partial y} \right) \\ \frac{\partial}{\partial x} \left( \frac{\partial V_z}{\partial z} \right) \end{array} \right\}$$

Update equation:

$$V_x(i, j, k) \leftarrow V_x(i, j, k) + \tau \frac{\partial}{\partial x} (\tilde{\nabla} \cdot \tilde{V}) \quad \tau \approx dx * dx$$

divergence. Because the boundary points were not precisely located on the boundary, their parallel component need not have been identically zero. The algorithm applied an exponential damping to the velocity component so that the component was reduced according to its distance from the boundary. These algorithms were implemented in C++ on a Silicon Graphics (SGI) Élan Indigo

computer. The *Explorer* program was used for the user interface and surface rendering program.

## RESULTS

Figure 3 shows streamlines generated by a sequence of algorithm runs using the curved tube flow phantom data.

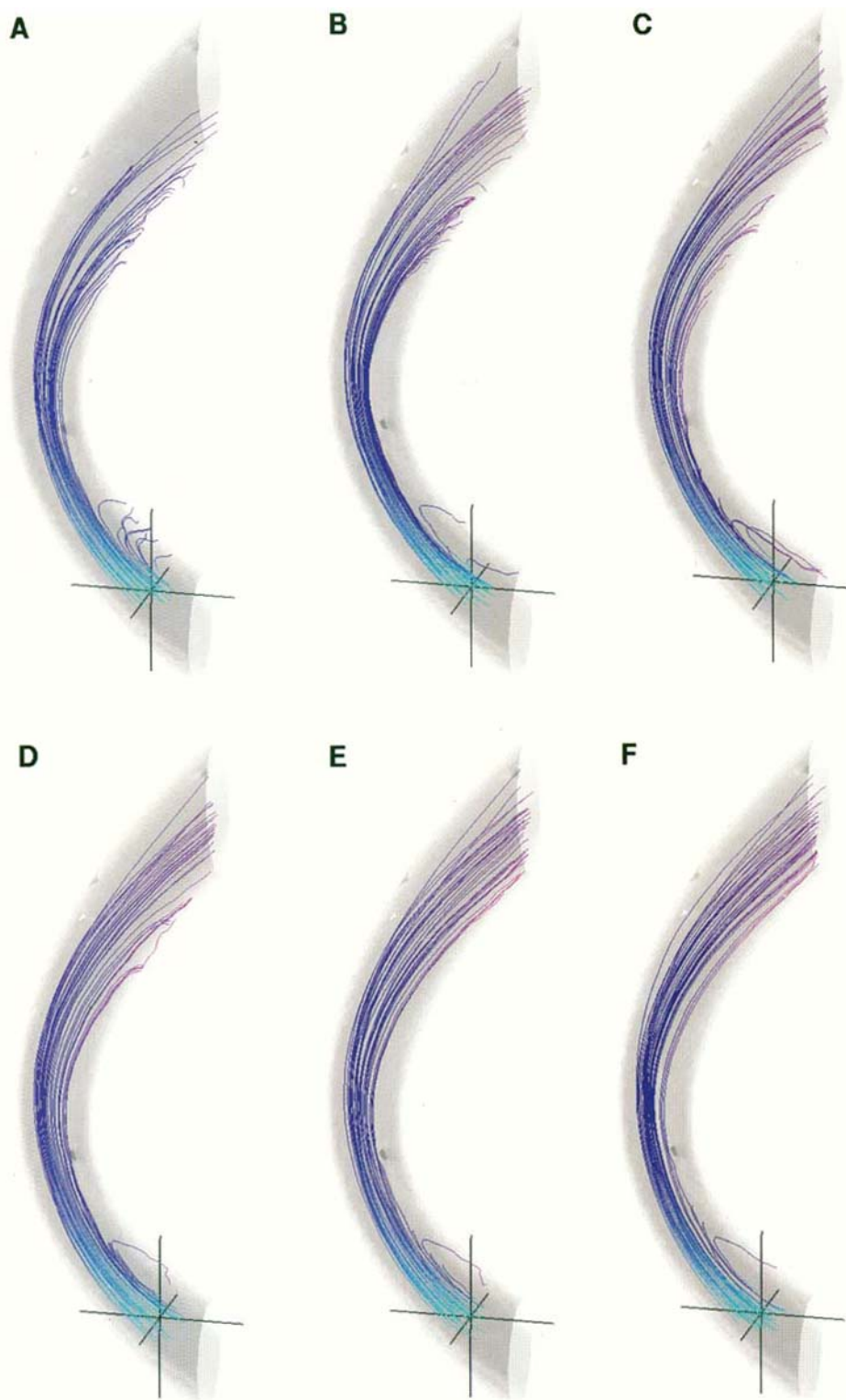


FIG. 3. Streamlines derived from phase contrast velocity data of curved-tube flow phantom: (A) Streamlines from unprocessed data. (B) Result of background correction. (C) Result of divergence correction. (D) Result of repeat background correction. (E) Result of flow-through-wall and divergence correction. (F) Result of repeat background correction. Color transitions are blue  $\rightarrow$  purple  $\rightarrow$  red  $\rightarrow$  yellow  $\rightarrow$  green, a sequence derived from linear tradeoff of blue to red, then red to green. At constant velocity there is linear passage of the color through these transitions.

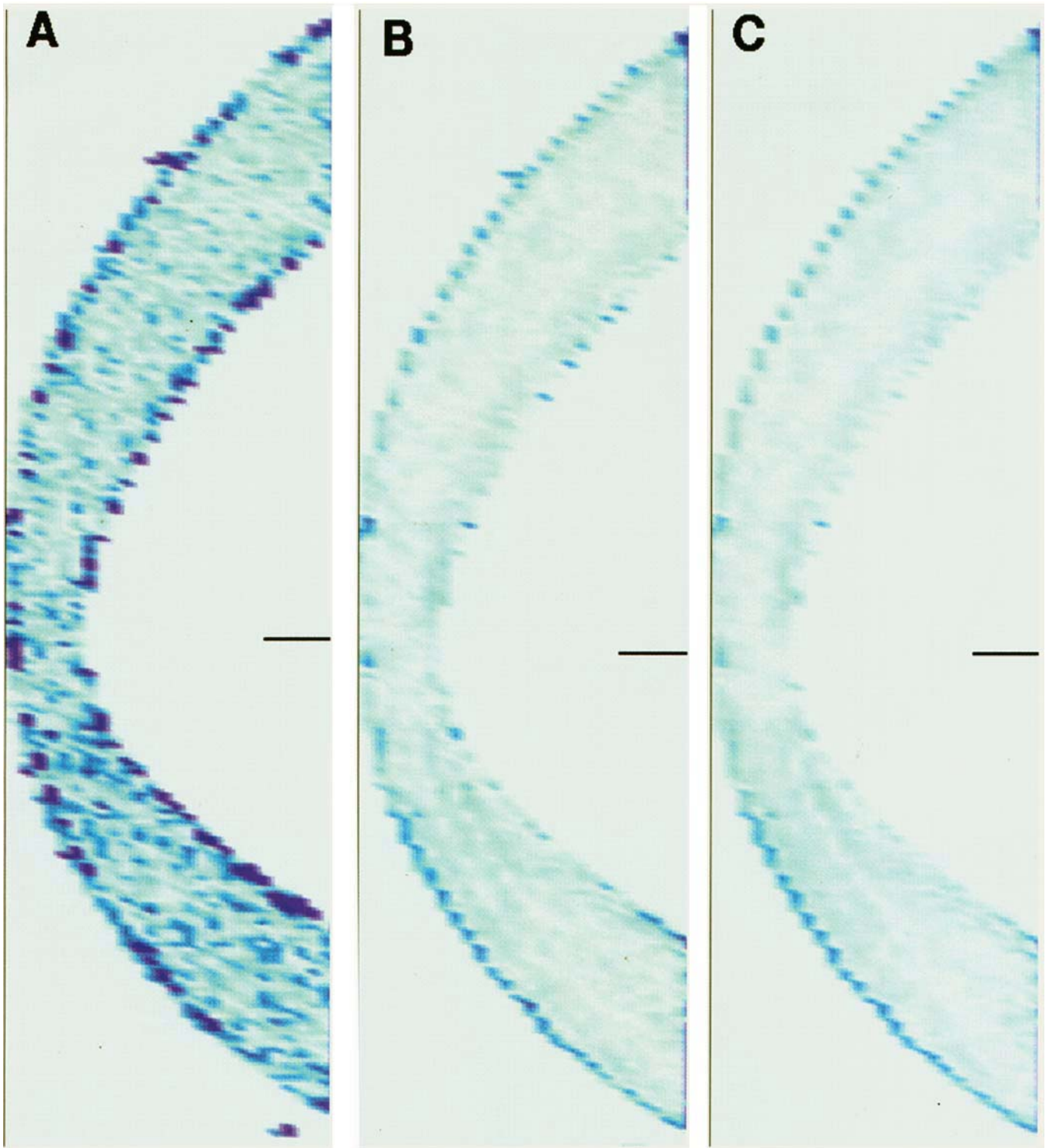


FIG. 4. Divergence correction: Slice through long axis of tube. Colormap: dark green (high divergence) to light green (low divergence). (A) initial data (B in Fig. 3). (C) After 10 iterations. (D) After 15 iterations (C in Fig. 3).

Background correction was used initially on the raw data because it provided global alignment of the velocity field to the vessel. An initial background correction was applied first using only the vessel wall constraint, then run again with the cross-sectional surface constraints to produce B. After divergence correction (C), background correction was used to eliminate remaining constant di-

vergence (D). After flow-through-wall correction, divergence and background corrections were used to restore zero divergence (E, F). The number of iterations varied for each step and algorithm type. Iterations were stopped when appreciable changes in the streamlines were not generated. The background correction used nine iterations to produce B. The divergence correction algorithm



used 15 iterations and 5 iterations to produce C and E, respectively. Figure 4 shows typical reductions in the divergence using this algorithm. Background correction required only one iteration to solve the least squares equation. Zeroing the velocity parallel to the wall gradient in the flow-through-wall correction required only one iteration.

Figure 5 graphs the improvement of the streamlines measured by a decrease in the number of streamlines passing through the vessel wall, and by the standard deviation of the mean flow through the cross sections. The background correction consistently provided the greatest reduction in flow standard deviation ( $4.95 \rightarrow 0.1$  in  $A \rightarrow B$ , and  $0.13 \rightarrow 0.08$  in  $E \rightarrow F$ ). This result was expected because the background correction selects the background to make the cross-sectional flows equal. The divergence correction ( $B \rightarrow D$ ) provided improvement in the streamlines ( $17\% \rightarrow 12\%$ ) but did not substantially reduce the cross-sectional flow standard deviations ( $0.15 \rightarrow 0.13$ ). Divergence correction was expected to improve both criteria. However, the flow-through-wall correction, followed by divergence and background correction, produced the greatest reduction in errant streamlines ( $12\% \rightarrow 4\%$  in  $D \rightarrow F$ ). This result was expected since the flow-through-wall correction eliminated the velocity components perpendicular to the wall at the boundary points.

Figure 6 shows results of a similar sequence of algorithm runs using left carotid artery velocity data. A shows streamlines from the unprocessed velocity field. B shows the streamlines after background correction. C shows the streamlines after divergence correction and subsequent background correction. D shows streamlines after flow-through-wall correction and subsequent divergence and background correction. Streamline improvements were similar to what was obtained in the phantom. Figures 7A and 7B display the divergence of the velocity field,  $\nabla \cdot \vec{V}$ , before and after application of the divergence correction algorithm (10 iterations). Within each carotid vessel, the algorithm reduced the divergence from 45% to 6% of the divergence of pixels in stationary tissue with-

in the neck. Figure 8 shows streamlines through the left carotid bulb of a normal subject. The streamlines show passage through the bulb of separate fast and slow flow channels.

## DISCUSSION

2-D arrow-maps and particle traces have been advocated for visualizing flow patterns (7). 3-D streamlines are a natural extension of these techniques. The 2-D techniques present only a single slice of velocity data at one time, so the observer must mentally merge the slices to visualize the flow pattern. 3-D image processing is necessary to provide temporally resolved, 3-D perspectives. Other algorithms have been published for generating streamlines that are a) consistent with fluid dynamical constraints and b) derived from experimentally acquired 3-D velocity fields (8). Doppler ultrasound velocity data was obtained from a hydraulic bench setup providing better than 1 mm in-plane resolution in a Plexiglas-stenosis model. The boundary of the stenosis model was known exactly and boundary conditions were imposed on a cartesian grid at their exact location. The divergence free constraint was written as coupled first order differential equations in spatial coordinates involving stream functions that were constant along streamlines. The streamlines were generated directly from these coupled equations. These formulae produced streamlines with the same desirable properties as the formulae reported in the present paper, but relied on prior knowledge of the precise location of the model wall. Unfortunately, the precise geometrical arrangement of their bench setup rarely is duplicated *in vivo*. Formulae were developed for axisymmetric 3-D velocity field only, not a general 3-D velocity field. The algorithms presented in the present paper can be applied to analysis of 3-D *in vivo* vessel data having arbitrary geometric orientation and shape relative to the cartesian grid on which the data was acquired.

The background correction adjusted the flow so that the net flow through the wall was zero, i.e., there was equal flow into and out of the vessel through the wall. It did not eliminate flow-through the wall locally at all boundary points, as did the flow-through-wall correction. Numerical stability of the divergence correction algorithm arises from the fact that the updated term, e.g.,  $V_x(i, j, k)$ , for each component of velocity does not appear in subsequent equations at each grid point. Convergence of the algorithm has not been proven mathematically, but was achieved in practice.

These algorithms will not improve the spatial and temporal resolution of the unprocessed velocity data. They will not necessarily bring the flow field closer to the unknown actual velocity field. For example, it is not possible to restore measured velocity to higher values in a region of rapidly changing velocities where readings may be damped by the data acquisition process. The numerical process of suppressing sources and sinks that occur in experimental velocity data may distort the data in other ways. However, the divergence correction algorithm was not biased toward lower velocities, as might have been expected. Simply shifting the velocities toward zero at each

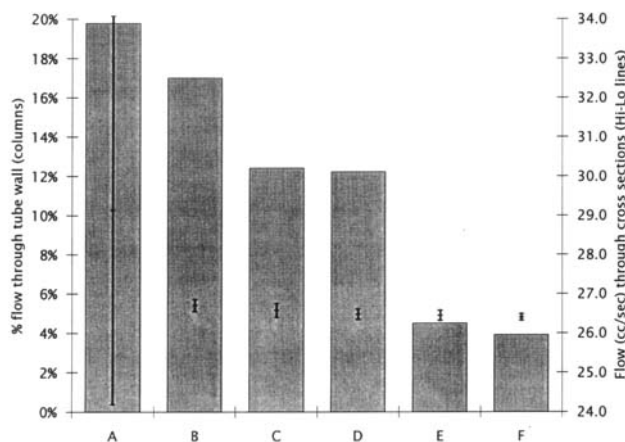


FIG. 5. Quantitative measurements of curved tube flow streamlines: Columns: Percentage of streamlines passing through the vessel wall, Hi-Lo lines: mean and standard deviation of the mean flow through multiple cross sections.

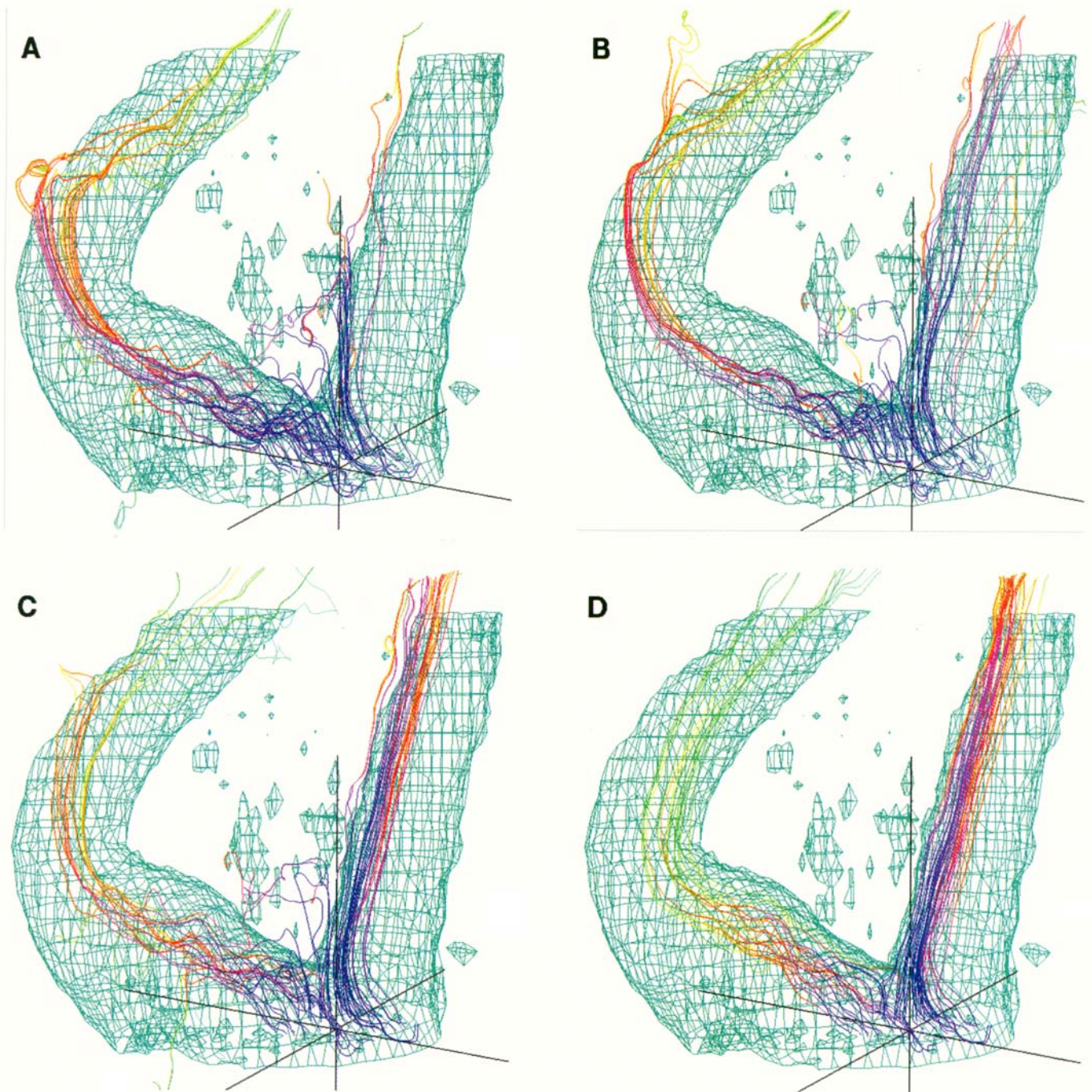


FIG. 6. Streamlines derived from phase contrast velocity data at carotid artery bifurcation. (A) Streamlines from unprocessed data. (B) Result of background correction. (C) Result of divergence correction, followed by repeat background correction. (D) Result of flow-through-wall correction, followed by repeat divergence and background corrections. Color transitions are the same as in Fig. 3.

voxel would have reduced the divergence, but the algorithm developed here reduced the gradient of the divergence and velocity vectors were increased or decreased with equal probability. Streamlines were generated using a small but fixed time step for first order velocity field integration. These first order forward integration algorithms often fail in tracking streamlines through complex flow patterns (9). These algorithms can be replaced by ones with variable order and variable step size to improve

tracking, but the added complexity increases the time to generate the streamlines and can impair interactive use. Streamlines based on the intersection of orthogonal stream surfaces automatically satisfy the divergence free constraint, are computed rapidly, and track streamlines through complex flow patterns.

The experiments did not test whether measurement accuracy improved. Previous work in phantoms showed that accuracy of net flow is significantly improved by



FIG. 7. Magnitude of divergence of velocity field across axial slice (A) before, and (B) after application of the divergence correction algorithm using 10 iterations. (A) shows that the unprocessed velocity data within the vessels has a smaller divergence compared with the nonflowing parts of the image. (B) shows that the algorithm further reduces the divergence in these vessels. Reduced divergence means that unphysical sources and sinks have been suppressed. Small caps A/P and R/L indicate anterior/posterior, left/right, respectively.

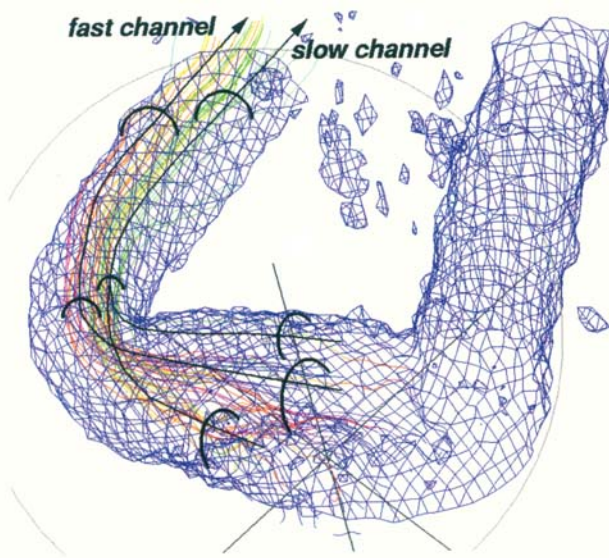
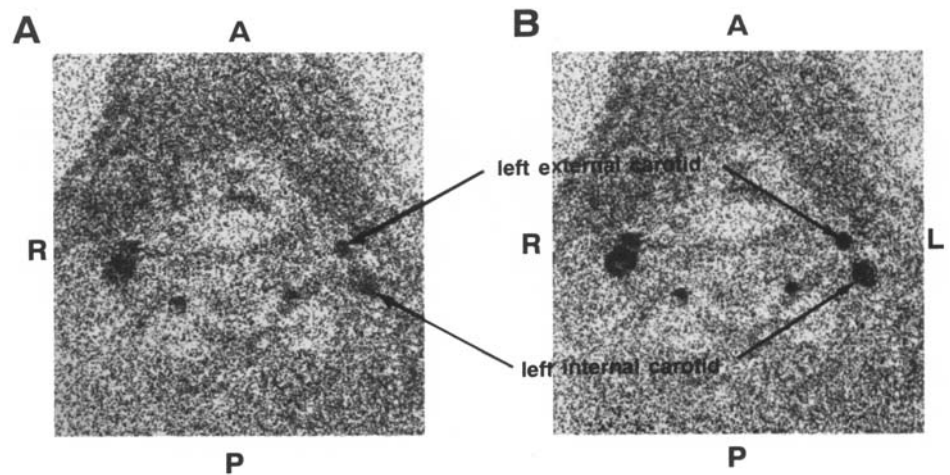


FIG. 8. Streamlines through the carotid bulb, derived from same sequence of algorithm runs as in Fig. 6, showing conjectured fast and slow channels of blood flow. Streamline color records time-of-arrival. Color transitions are same as in Figs. 3 and 6.

background correction (3, 4). Therefore, the carotid artery net flow measurements probably improved after background correction. The experiments did not show whether subtle details of the actual blood flow patterns were more accurately portrayed after processing. The algorithms greatly improved the coarse appearance and realism of the streamlines, since they dictated no passage of streamlines through vessel walls, and no intraluminal sources and sinks. The streamlines were more accurate in the sense that they were made to obey these physical requirements with minimal adjustment of the data. An alternative modality for velocity or streamline generation is needed to determine if the algorithms improve the depiction of a flow pattern's subtle details. *In vivo* comparisons of flow patterns are not possible at present because an alternative *in vivo* modality does not exist. An alternate MR pulse sequence may provide the best comparison. For example, in the ascending aorta, the timing and extent of recirculating flow streamlines calculated from axial gated 3-D velocity encoded images could be

compared with the images from gated 2-D coronal sequences. Multistripe tagging could be used to visualize streamlines directly in amplitude images (10).

Ungated data cannot portray many physiologically interesting flow patterns. Recirculating flow in the carotid bulb cannot be visualized without gating, nor can diastolic recirculating flow in the mid-ascending aorta providing blood to the coronary arteries. In the carotid bulb, recirculation is time-averaged by the pulse sequence and is displayed as slow flow. Velocity fields obtained from ungated scans should obey fluid dynamics' conservation laws. Independent phase contrast flow measurements are statistical averages of the flow over the RR interval (11, 12). Since the divergence is a linear operator, the average velocity field should have zero divergence. However, the standard deviation of velocity measurements is much larger with nongated velocity data relative to data obtained with full gating. Therefore, larger corrections will be needed to make the divergence zero with non-gated compared to fully gated data. Momentum conservation, i.e., the Navier-Stokes equation, is given by a differential equation that includes a term with the square of the velocity at each point. Since this term is nonlinear, the average velocity data obtained in nongated sequences may not satisfy this equation. Momentum conservation was not used for processing nongated data. An algorithm that modifies time-resolved velocity fields to minimize the Navier-Stokes equation error is under development for future studies using gated velocity data. Existing background and divergence correction algorithms are valid for gated data at each instant of time because the fluids are modeled as incompressible.

Streamline visualization has potential for routine clinical application. The formation of atherosclerosis correlates best with chronic low shear regions at vessel branch points (1). Streamlines and particle tracking have been used in computer simulation and laboratory experiments to identify these regions. Streamlines have been used to better visualize and quantify pre- and post-stenotic pulsed Doppler measurements in laminar and turbulent flow (8), (13–15). Using Indium-111 labeled transferrin platelets, arterial thrombus formation was correlated with flow patterns described with nonparallel streamlines (16, 17).



Spatial concentration profiles of blood constituents have been related to the geometric arrangement of streamlines (18, 19). In the carotid artery bifurcation, streamlines have been used to visualize reverse and "wavy" flow patterns that occurred in locations coinciding with atherosclerotic lesions (20). While the correlation of specific flow patterns and atherogenesis at vessel branching has been established, the mechanism of atherogenesis is not completely understood. A central question is the mechanism whereby physical properties of the flow, i.e., shear stress and pressure, disrupt normal cellular metabolism and lead to accumulation of cholesterol and lipid in the intimal layer of the vessel wall, and to proliferation of myocytes in the medial layer (1). Since abnormal flow patterns are part of the ideology of atherosclerosis, the display method should show these flow patterns clearly. Points of separation of parallel streamlines, and recirculation regions immediately distal to these points should be quickly identified in the 3-D display. In conjunction with independent measurements of atherosclerosis extent, clear visualization of the flow patterns could lead to new correlation with atherosclerosis formation. Intricate flow patterns have also been observed in the ascending aorta in formation of coronary artery flow. Visualizing these flow patterns may reveal new mechanisms underlying insufficient coronary artery flow. Generation of streamlines appears to be a valuable image processing enhancement for detection and understanding of cardiovascular disease mechanisms.

## REFERENCES

1. R. M. Nerem, M. J. Levesque, Fluid mechanics in atherosclerosis, in "Handbook of Bioengineering," (R. Skalak, S. Chein, Eds.), McGraw-Hill, New York, 1987.
2. S. Napel, D. H. Lee, R. Frayne, B. K. Rutt, Visualizing three-dimensional flow with simulated streamlines and three-dimensional phase-contrast MR imaging. *J. Magn. Reson. Imaging* **2**(2), 143–153 (1992).
3. M. H. Buonocore, Flow measurement using variable velocity encoding in the RR interval. *Magn. Reson. Med.* **29**, 790–795 (1993).
4. M. H. Buonocore, H. Bogren, Factors influencing the accuracy and precision of flow measurements using velocity encoded phase images, *Magn. Reson. Med.* **26**, 141–154 (1992).
5. T. E. Conturo, G. D. Smith, Signal-to-noise in phase angle reconstruction: dynamic extension using phase reference offsets, *Magn. Reson. Med.* **15**, 420–437 (1990).
6. G. R. Cokelet, The rheology and tube flow of blood, in "Handbook of Bioengineering," (R. Skalak, S. Chein, Eds.), McGraw-Hill, New York, 1987.
7. R. H. Mohaiddin, G. Z. Yang, P. J. Kilner, D. B. Longmore, Visualization of flow by vector analysis of multidirectional cine MR velocity mapping: technique and application. *J. Magn. Reson. Imaging* **3**(P), 26 (1993).
8. N. Chahed, P. Peronneau, A. Delouche, B. Diebold, Velocity profiles and streamlines of a revolution post-stenotic flow. *Biorheology* **28**, 383–400 (1991).
9. D. N. Kenwright, G. D. A 3-D streamline tracking algorithm using dual stream functions. "Proceedings Visualization '92" (Cat. No.92CH3201-1). (Proceedings Visualization '92 (Cat. No.92CH3201-1), Boston, MA, USA, 19–23 Oct. 1992). Los Alamitos, CA, USA: IEEE Comput. Soc. Press, 1992. p. 62–8.
10. M. V. Icenogle, A. Caprihan, E. Fukushima, Mapping flow streamlines by multistripe tagging. *J. Magn. Reson.* **100**, 376–381 (1992).
11. M. H. Buonocore, L. Gao, Experimental study of the effects of 'fractional' gating on flow measurement accuracy and precision, in "Poster, 10th Annual Meeting, SMRI, 1992."
12. M. B. M. Hofman, M. Kouwenhoven, M. Sprenger, A. C. van Rossum, J. Valk, N. Westerhof, Nontriggered magnetic resonance velocity measurement of the time average of pulsatile flow. *Magn. Reson. Med.* **29**, 648–655 (1993).
13. T. Utsunomiya, T. Ogawa, H. A. Tang, R. Doshi, D. Patel, M. Quan, W. L. Henry, J. M. Gardin, Doppler color flow mapping of the proximal isovelocity surface area: a new method for measuring volume flow rate across a narrowed orifice. *J. Am. Soc. Echocardiogr.* **4**(4), 338–348 (1991).
14. F. Recusani, G. S. Bargiggia, A. P. Yoganathan, A. Raisaro, L. M. Valdes-Cruz, H. W. Sung, C. Bertucci, M. Gallati, V. A. Moises, I. A. Simpson, A new method for quantification of regurgitant flow rate using color Doppler flow imaging of the flow convergence region proximal to a discrete orifice. An in vitro study. *Circulation* **83**(2), 594–604 (1991).
15. T. Tamura, R. S. Cobbold, K. W. Johnston, Quantitative study of steady flow using color Doppler ultrasound. *Ultrasound Med. Biol.* **17**(6), 595–605 (1991).
16. R. Lassila, J. J. Badimon, S. Vallabhajosula, L. Badimon, Dynamic monitoring of platelet deposition on severely damaged vessel wall in flowing blood. Effects of different stenoses on thrombus growth. *Arteriosclerosis* **10**(2), 306–315 (1990).
17. L. Badimon, J. J. Badimon, Mechanisms of arterial thrombosis in nonparallel streamlines: platelet thrombi grow on the apex of stenotic severely injured vessel wall. Experimental study in the pig model. *J. Clin. Invest.* **84**(4), 1134–1144 (1989).
18. F. W. Rong, R. T. Carr, Dye studies on flow through branching tubes. *Microvasc. Res.* **39**(2), 186–202 (1990).
19. J. E. Hokkanen, A two-fluid model for hematocrit distribution in microvascular networks. *Med. Phys.* **16**(3), 319–325 (1989).
20. M. Nazemi, C. Kleinstreuer, J. P. Archie Jr., Pulsatile two-dimensional flow and plaque formation in a carotid artery bifurcation. *J. Biomech.* **23**(10), 1031–1037 (1990).